Soil resistance during vibratory pile installation
Experimental findings from lab-scale tests

Martinelli, Mario; Tsetas, Athanasios; Fărăgău, Andrei B.; Metrikine, Andrei; Tsouvalas, Apostolos

DOI
10.1016/j.soildyn.2025.109692

Publication date
2025

Document Version
Final published version

Published in
Soil Dynamics and Earthquake Engineering

Citation (APA)
Martinelli, M., Tsetas, A., Fărăgău, A. B., Metrikine, A., & Tsouvalas, A. (2025). Soil resistance during vibratory pile installation: Experimental findings from lab-scale tests. *Soil Dynamics and Earthquake Engineering*, *199*, Article 109692. https://doi.org/10.1016/j.soildyn.2025.109692

Soil Dynamics and Earthquake Engineering 199 (2025) 109692

Contents lists available at ScienceDirect

Soil Dynamics and Earthquake Engineering

journal homepage: www.elsevier.com/locate/soildyn

Soil resistance during vibratory pile installation: Experimental findings from lab-scale tests

Mario Martinelli [a,b,*], Athanasios Tsetas [b], Andrei B. Fărăgău [b], Andrei Metrikine [b], Apostolos Tsouvalas [b]

[a] Geo-Engineering Unit, Deltares, Boussinesqweg 1, Delft, 2629 HV, The Netherlands
[b] Faculty of Civil Engineering and Geosciences, Delft University of Technology, Stevinweg 1, Delft, 2628 CN, The Netherlands

ARTICLE INFO

Keywords:
Vibratory pile driving
Pile–soil interaction
Lab experiments
Friction fatigue
CPT-based methods

ABSTRACT

The increasing size of offshore wind turbine foundations necessitates innovative approaches for monopile installation. Traditionally performed through impact driving, the challenges of large stresses induced on the monopile and high levels of underwater noise emissions have driven a shift toward vibratory installation methods. This study investigates the vibro-installation process of steel tubular piles in dense saturated sand through controlled lab-scale experiments. The experiments systematically varied penetration rates and driving frequencies to analyze the interaction between the piles and the surrounding soil. The results reveal critical insights into the influence of vibratory parameters on soil resistance and pile drivability, with a specific focus on the response of the pile tip and shaft under different conditions. These findings contribute to improved predictive models for monopile installation, addressing data gaps in offshore conditions and supporting the optimization of vibratory techniques for sustainable and cost-effective wind energy development.

1. Introduction

Monopiles are currently the most common foundation type for offshore wind turbines, consisting of a single steel pipe driven into the seabed to support the wind turbine tower [1]. Traditionally, monopiles have been installed through impact hammering, where a large impact hammer repeatedly strikes the pile until it reaches the required penetration depth [2]. However, for large-diameter piles, impact driving can become impractical due to the over-sized structures needed to withstand the high stresses caused by hammering and the significant underwater noise emissions generated [3].

In recent years, vibro-driving methods have been explored as a potential alternative for the offshore installation of monopiles, as well as even larger caisson/bucket-like cylindrical structures [4–7]. This technique employs a hydraulically powered vibratory device to induce vertical vibrations, which reduce the soil resistance around the pile, allowing easier penetration [8]. Vibro-driving offers potential advantages, such as reduced installation time, lower noise emissions, and cost savings, particularly for large-diameter monopiles. However, despite these benefits, the application of vibro-driving in full-scale offshore wind projects remains limited. Most offshore installations still rely on impact hammering, often in combination with vibratory techniques, rather than vibro-driving as a standalone installation method. Previous projects, such as Formosa I [9], Formosa II [10], Kaskasi II [11], and Riffgat [12], have used vibro-assisted driving but not as the sole installation method. Additionally, ongoing projects such as Coastal Virginia [13], Hai Long [14], Moray West [15], and Yunlin [16] highlight the challenges of fully certifying vibro-installed monopiles. Several uncertainties hinder the widespread adoption of vibro-driving, including the lack of well-established design methods, the difficulty of defining conservative installation approaches, and practical constraints such as the need for multiple power packs, which reduce deck space and impact logistics.

Next to the ongoing vibro-driving studies, a series of other innovative solutions are also investigated, sharing the common goal of advancing more environmentally-friendly and efficient methods for monopile installation. A rotational excitation is utilized in methods such as the axial-torsional vibratory driving (i.e. GDP method) [17], and the rotational installation of helical/screw piles [18]. Additionally, water-jetting – with or without axial loading – presents another approach for monopile driving [6,19]. Finally, we note that developments in the area of impact piling, yet focused on mitigating its adverse environmental effects are also actively researched, such as near-field noise mitigation systems [20] and optimized hammer design [21].

This paper investigates the vibro-installation of tubular piles through a series of lab-scale experiments conducted at the Deltares

---

* Corresponding author at: Geo-Engineering Unit, Deltares, Boussinesqweg 1, Delft, 2629 HV, The Netherlands.
E-mail address: mario.martinelli@deltares.nl (M. Martinelli).

https://doi.org/10.1016/j.soildyn.2025.109692
Received 12 March 2025; Received in revised form 18 July 2025; Accepted 22 July 2025

laboratory as part of the SIMOX Joint Industry Project [22]. The study provides critical insights into the interaction between pile and soil during vibratory driving, focusing on the effects of driving frequency, penetration speed, and friction fatigue on soil reaction. The findings contribute to better comprehending the physics of vibro-driving by elucidating the mechanisms governing tip and shaft reactions and evaluating predictive models for friction fatigue. The practical implications highlight the potential for optimizing vibratory driving as a more sustainable and efficient alternative for offshore monopile installation, while also emphasizing the need for further research to address current limitations.

The paper is divided into five sections, followed by the conclusions. The first section reviews vibratory driving modeling approaches, highlighting current challenges and knowledge gaps. The second section details the lab testing program, including the experimental setup, instrumentation, and testing conditions. The third section presents key results, focusing on pile and soil response during installation. The fourth and fifth sections analyze the response of the tip and shaft during driving, respectively. Finally, the conclusions summarize the key findings of this study and outline recommendations for future research.

2. Vibratory driving modeling

The challenge of installing large-diameter monopiles has recently led to increasing research efforts to comprehend the physics of the pile installation process and to develop reliable prediction tools. The majority of these developments mostly focused on impact piling, in particular aspects such as the CPT-based approaches for characterizing the static resistance to driving (SRD) [23]. Naturally, vibratory driving approaches have adopted components of the impact piling models, as the latter preceded in the field of offshore monopile installation.

Presently, the available modeling approaches for vibratory pile driving can be broadly divided into two categories. The first category comprises high-fidelity models, including advanced constitutive model formulations for the soil material [24]. Significant insights can be obtained by these studies, both in terms of the soil behavior in the pile vicinity – where large strains and displacements occur – as well as in the computational frontier. The pile installation process serves as an excellent benchmark for testing new approaches and methods, as seen in studies using CEL [25,26] and MPM [27,28]. However, high-fidelity models have notable drawbacks, including their excessive computational cost, which makes them inapplicable yet for engineering applications. Additionally, their reliance on advanced constitutive soil models requires extensive laboratory testing to calibrate and determine a large number of soil parameters, which can introduce high uncertainty into the engineering solution.

The second category corresponds to medium-fidelity models, which can be considered more engineering-oriented and applicable to offshore engineering practice. Among these approaches, a significant part corresponds to adaptations of 1-D wave equation models from impact piling [29,30]. Furthermore, 1-D radial models have also been particularly developed for vibro-driving, modeling the pile as a rigid body and the soil as concentric rigid cylinders [31,32]. Finally, recent works encompass more physically accurate approaches for modeling the pile and the soil reaction to driving [33,34]. It is clear that ongoing and future works combining both numerical modeling and large-scale experiments (onshore and/or offshore) are necessary to validate such models and establish a reliable engineering-oriented framework for vibro-driving predictions.

3. Lab testing programme

This section describes the relevant part of the experimental campaign conducted at the Deltares laboratory in Delft, the Netherlands. All tests see several piles being installed in a large tank with dimensions of 9.0 *x* 5.5 *x* 2.5 m (length *x* width *x* depth), which was filled with soil to a depth of 2.4 m; a picture of the overall set-up from an elevated viewpoint is shown in Fig. 1. The characteristics of the filling soil are discussed in Section 3.1.

Throughout the testing program, different piles were used. The main pile studied in this paper was a steel pipe with an outer diameter of $D_\mathrm{p} = 0.32$ m, a total length of $L_\mathrm{p} = 2.0$ m, and a wall thickness of $t_\mathrm{p} = 4$ mm. The piles were installed to a depth of about 1.5 m into the ground, with a distance between the bottom of the tank and the pile tip of about 0.9 m, leaving approximately 0.5 m of the pile exposed above the ground level. The embedded length was $L_\mathrm{emb} = 1.5$ m, hence the $L_\mathrm{emb}/D_\mathrm{p}$ ratio was 4.6, which is considered representative for offshore monopiles.

The testing campaign consisted of four sets of tests: in the first three sets (#1, #2, and #3), the soil was compacted to a dense state (i.e. target relative density 70% to 90%), while in the final set (#4), the soil was prepared in a medium-dense state (i.e. target relative density 40% to 60%). All tests included not only pile installation but also the response of piles under lateral loading. For further details on the complete testing program and pile behavior under lateral loading, refer to [35].

This paper focuses exclusively on the installation of eight instrumented piles in dense sands, specifically: seven tests from set #1 (see Fig. 2), and one test from set #2. Fig. 2 shows the locations inside the tank where the piles were installed during Set #1 (T1–T7, where *T* stands for test), along with the CPTs, as well as the location of pile T8 installed in set #2. The details of the instrumentation applied to the piles are summarized in Section 3.2.

3.1. Soil properties

The tank used for the tests was filled with saturated Sibelco S90 sand [36], which is a medium-fine sand with high sphericity and subangular shape. The sand has a mean particle size of $d_{50} = 0.147$ mm, a coefficient of uniformity $C_u = 1.6$, and average maximum and minimum densities of 1.590 and 1.333 g/cm^3, respectively. The tank was filled in layers of approximately 50 cm that were individually compacted to the desired value using vibrating needles.

To assess the uniformity and homogeneity of the soil characteristics (e.g., relative density) in the tank, several CPTs were performed at various locations, including directly adjacent to each pile installation site, using a cone with a standard tip area of 10 cm^2 equipped with a sleeve friction measurement system. The positions of the CPTs in the tank for set #1 are shown in Fig. 2. These CPTs were performed exclusively prior to the pile installation tests, ensuring that their penetration did not disturb soil conditions influenced by the driving process. The CPT locations were carefully selected to avoid overlapping with the pile positions, maintaining a minimum distance of at least one pile radius from the pile wall. Although some localized disturbance from CPT insertion cannot be entirely excluded, its impact is considered negligible due to the small diameter of the cone, the limited number of CPTs near each pile, and the deliberate spatial separation maintained during test planning.

The evolution of the cone resistance with depth is shown for some CPT-logs, located near T1 and T6, in Figs. 3 and 4, respectively. In all CPTs, the friction ratio (R_f), defined as the ratio between the friction sleeve resistance and the cone resistance at the same depth, ranges between 0.3% and 0.5%. The figures also show the relative density in the soil domain, estimated from the CPT measurements, as direct measurement of relative density was not possible. The estimation followed the procedure outlined in [37].

Overall, the estimated relative density increases with depth, reaching a constant value of about 70%–75% at depths greater than 1 m. This value remains consistent across almost all CPTs adjacent to the piles discussed in this paper, highlighting the effectiveness of the preparation procedure. However, some variability in relative density is observed at

Fig. 1. The first pile placed on the soil surface prior to installation in the large soil tank of Deltares.

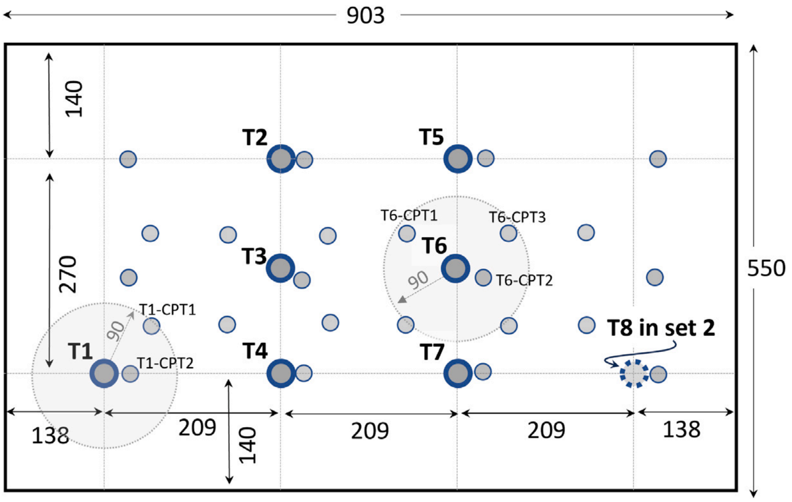

Fig. 2. The location of CPTs and piles (T1–T7) for set #1, and pile T8 for set #2.

shallow depths for certain piles, particularly those located near the left or right tank walls. For example, in Fig. 3, the soil near T1 at shallow depths is loose to medium-dense, as indicated by the different values of cone resistance between $T1 - CPT_1$ and $T1 - CPT_2$.

When back-analyzing the pile response, discussed in Sections 5 and 6, a representative value of cone resistance is adopted. In this paper, the average value of the CPT measurements from all CPTs located within 90 cm of the center of the pile location was chosen. This procedure is illustrated in Fig. 2 for T1 and T6, where a circle with a radius of 90 cm is depicted, highlighting all relevant CPTs that fall within this area. The corresponding average CPT measurements for these two piles are presented in Figs. 3 and 4.

3.2. *Installation equipment and instrumentation*

For all tests presented in this paper, the monopile was instrumented to record its dynamic response throughout the driving process. The pile vibrations were measured using a combination of tri-axial accelerometers and uni-axial (vertical direction) strain gauges positioned at three longitudinal positions (i.e., rings). Fig. 5(a) presents a schematic of the sensor positions. The top ring positioned at 0.3 m from the pile top has 4 uni-axial strain gauges (0, 90, 180, and 270 degrees along the circumference) and 2 tri-axial accelerometers (0 and 180 degrees). The middle ring (at 1.0 m from the pile top) and bottom ring (at 0.15 m

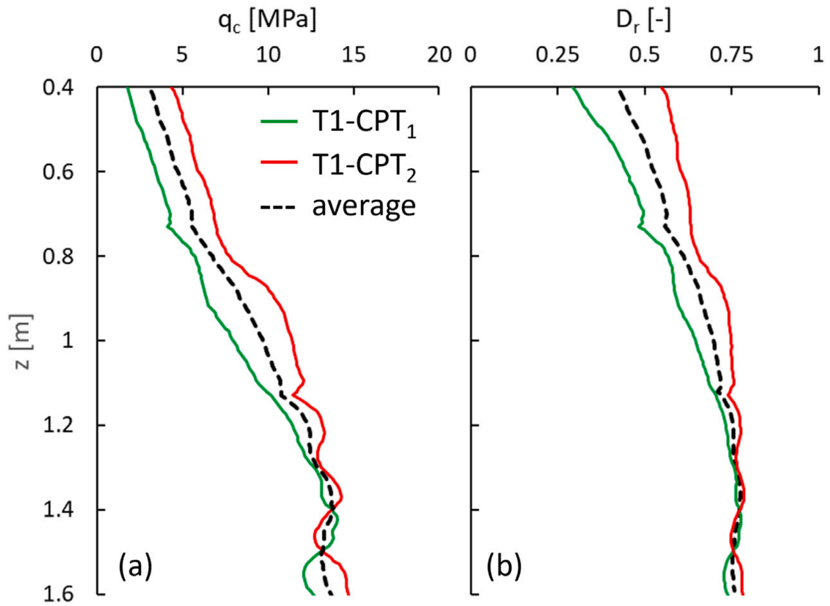

Fig. 3. Test 1: (a) cone resistance as a function of depth and (b) the corresponding relative density.

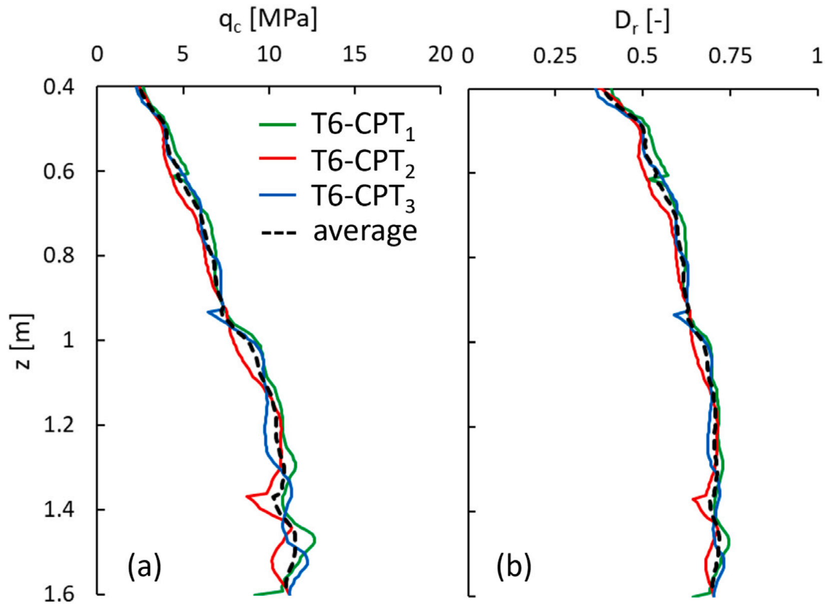

Fig. 4. Test 6: (a) cone resistance as a function of depth and (b) the corresponding relative density.

from the pile tip) were both instrumented with 2 uni-axial strain gauges (0 and 180 degrees).

Additionally, the bottom ring was equipped with total stress sensors, in particular Kyowa PS-2KC and PS-10KC with a capacity of 200 kPA and 1 MPa, respectively. These sensors were placed along the internal and external faces of the pile, to measure the total stress exerted on the pile wall. A close-up photograph is shown in Fig. 5(b). The total stress sensors allowed for detailed observations of the stress changes between the inner and outer pile shaft during the installation process, contributing to a better understanding of the interaction between the pile and the surrounding soil. It is worth noticing that the total stress sensors were not installed on all piles, but only for one pile in the testing program (i.e., T8 in Table 1).

During installation tests, a load cell was placed between the lower end of the crane and the vibro-hammer to measure the weight of the system suspended by the crane and detect whether the pile is free-hanging (zero crane load) or if its weight is (partially) carried by the overhead crane. Mounted next to the pile, a laser sensor measured the vertical displacement in order to compute the penetration speed and monitor the vertical movements of the pile during installation. The load cell on the crane is a U9 load cell by Hottinger with a capacity of 20 kN. The laser was a Demetix DPE-30-500 Laser Distance Sensor.

The hydraulic vibro-hammer used was the model APE-23, with an eccentric moment of 1.3 kg·m and an operational frequency up to 37.5 Hz. The vibro-hammer was connected to the pile through a bolted connection. During installation, a guiding system was used to ensure the pile verticality, as well as to prevent the pile-hammer setup from rotating. An accelerometer was placed on the vibratory hammer to measure its acceleration profile as well as to compute the vibratory frequency during installation. A closer view of the pile, vibro-hammer and crane assembly is provided in Fig. 6.

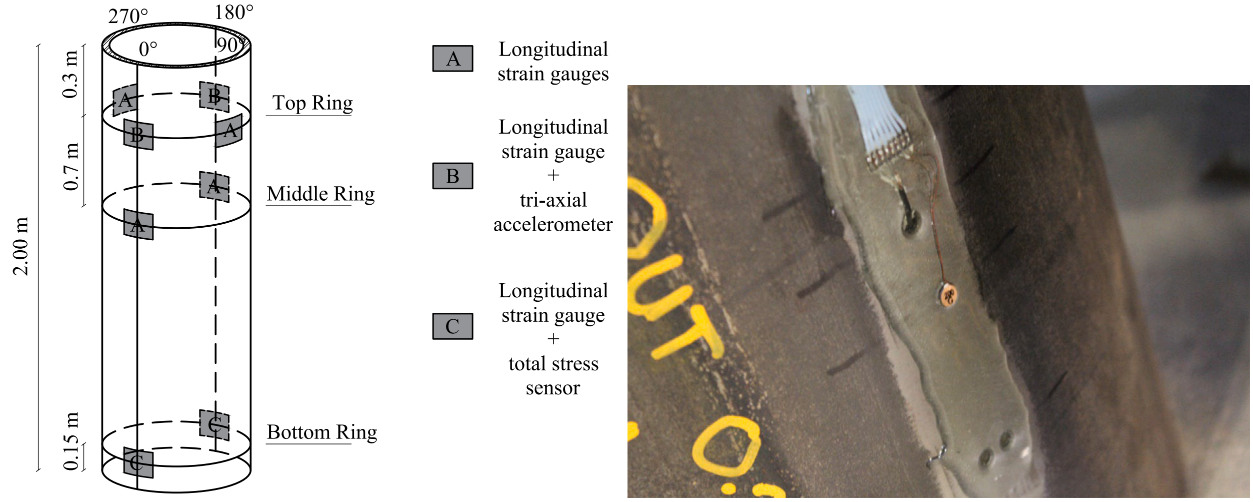

(a) **(b)**

Fig. 5. (a) Schematic representation of the pile instrumentation. (b) A close-up photograph of the total pressure sensor installed at the bottom ring of the pile.

Fig. 6. A close-up view of the pile, vibro-hammer and crane assembly, at the end of installation.

3.3. Test program

The influence of the driving frequency and the crane-lowering speed on the drivability was investigated. The crane had two possible lowering speeds during installation: 10 mm/s (slow speed) or 110 mm/s (fast speed). Additionally, installations were performed at three target driving frequencies: low (~ 19 Hz), medium (~ 23 Hz) and high (~ 35 Hz). Table 1 presents the combination of these two parameters for all the tests conducted.

Table 1
The parameters varied between the 8 tests, namely the driving frequency and the crane lowering speed.

Test	Set	Driving frequency	Crane speed
T1	1	High	Slow
T2	1	High	Fast
T3	1	Medium	Slow
T4	1	Medium	Fast
T5	1	Low/Medium	Slow
T6	1	Low	Fast
T7	1	Low/Medium	Slow
T8	2	Low	Slow

4. Selected test results

In this section, the results from T1 and T6 are discussed in more detail, as examples of slow and fast installation cases, respectively. Figs. 7 and 8 show the evolution in time of the pile penetration, and the envelopes of vibratory forces applied at pile head (F_h) and at the pile tip (R_t).

At the start of each test, the pile is lifted by the crane and positioned at the installation location. Gradually, the crane load is released, increasing the static force at the pile head – due to the hammer's weight – which causes the force at the pile tip to increase and the pile to penetrate into the ground until reaching an equilibrium configuration. The vibro-hammer is then activated, allowing the pile to penetrate further into the ground.

The vibratory forces, F_h and R_t, are computed as follows:

$$F_h = EA\varepsilon_h \tag{1}$$

$$R_t = EA\varepsilon_t \tag{2}$$

where E is the Young's modulus of the pile, A is the cross-section area of the pile, ε_h and ε_t are the axial strains at the pile head (i.e., top instrumented ring) and at the pile tip (i.e., bottom instrumented ring), respectively.

Figs. 7 and 8 show also the driving frequency in time, which was computed from the acceleration time series recorded at the pile head. The acceleration was then single and double integrated in time, and the cyclic velocity and cyclic displacements were computed; the quantities are high-pass filtered with a cut-off frequency set to 2 Hz, thus excluding the minor contribution of the monotonically increasing

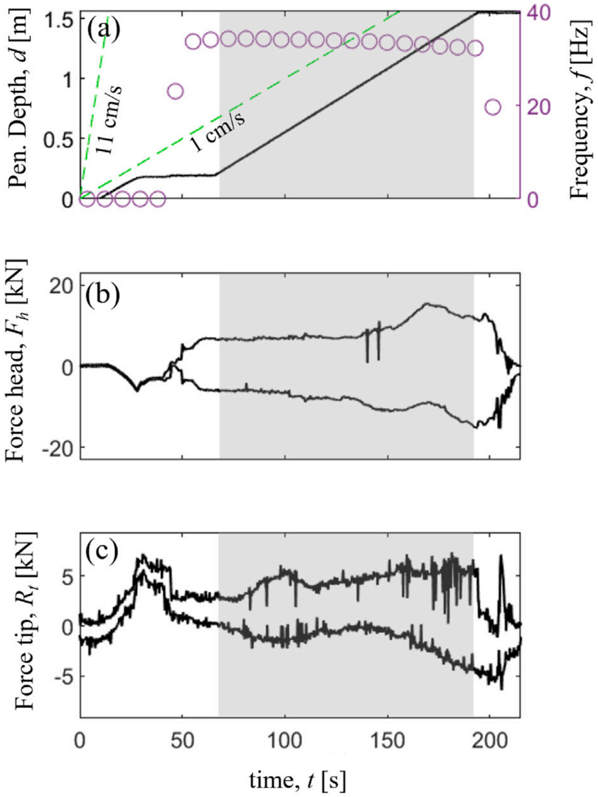

Fig. 7. Time-history response of pile T1: (a) Penetration, (b) envelope of maximum and minimum forces at the pile head, and (c) envelope of maximum and minimum forces at the pile tip. The gray background highlights the interval in which driving is ongoing.

penetration. Results are shown in Figs. 9 and 10 for T1, and in Figs. 11 and 12 for T6.

Each figure shows a shaded area, highlighting the period in the monitoring data that corresponds to pile installation, specifically when piles are driven into the ground. The vibro-hammer is also activated outside this shaded area, so dynamic forces are still applied to the pile; however, because the pile is held by the crane, so displacements are restrained.

The length of the pile is short, and the stiffness is sufficiently high to reasonably assume that the pile behaves as a rigid body for the driving frequencies considered herein. Therefore, the equilibrium of the forces acting on the pile is written as follows:

$$m_p \ddot{u}_p + R = F_h \tag{3}$$

where m_p is the pile mass (limited to the portion of the pile between the two stain gauges, at pile head and at pile tip), R is the pile driving resistance exerted by the soil, and $\ddot{u}_p$ is the pile acceleration, assumed to be identical to the acceleration measured at the pile head under the rigid-body behavior assumption.

The pile driving resistance (R) can be divided into the following two components, the pile tip resistance (R_t) and the pile shaft resistance (R_s). The latter one can be computed as follows:

$$R_s = F_h - R_t - m_p \ddot{u}_p \tag{4}$$

The time-history of the envelopes of the inertial force ($m_p \ddot{u}_p$), the pile driving resistance (R) and the pile shaft resistance (R_s) is shown in Figs. 13 and 14.

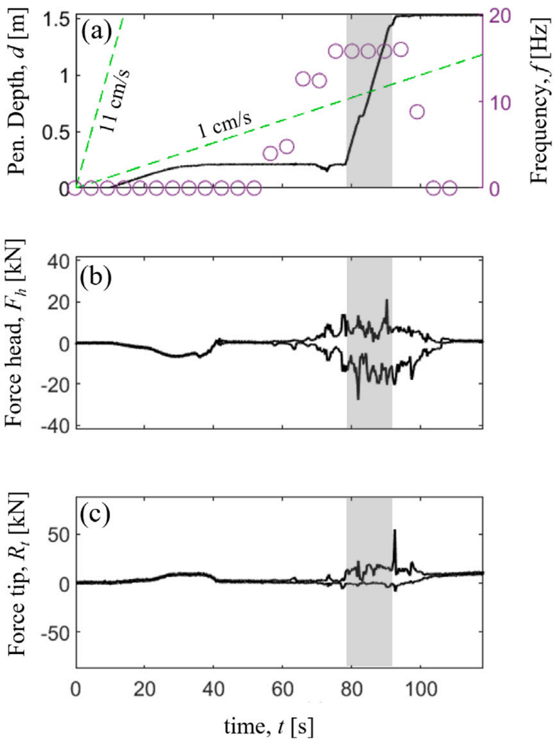

Fig. 8. Time-history response of pile T6: (a) Penetration, (b) envelope of maximum and minimum forces at the pile head, and (c) envelope of maximum and minimum forces at the pile tip. The gray background highlights the interval in which driving is ongoing.

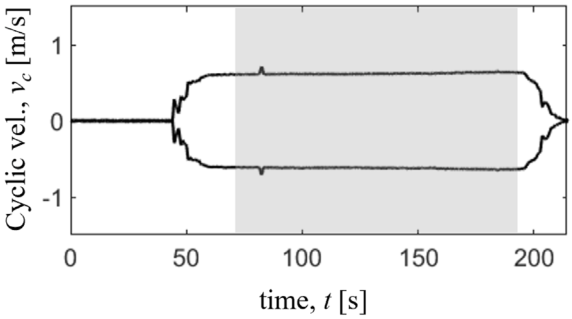

Fig. 9. Time-history response of pile T1: Envelope of maximum and minimum cyclic velocities. The gray background highlights the interval in which driving is ongoing.

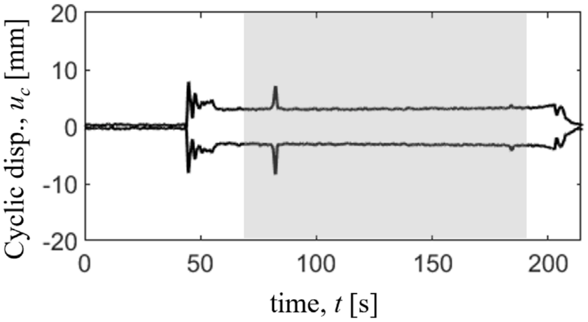

Fig. 10. Time-history response of pile T1: Envelope of maximum and minimum cyclic displacements. The gray background highlights the interval in which driving is ongoing.

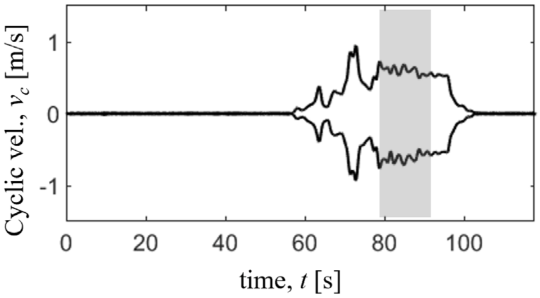

Fig. 11. Time-history response of pile T6: Envelope of maximum and minimum cyclic velocities. The gray background highlights the interval in which driving is ongoing.

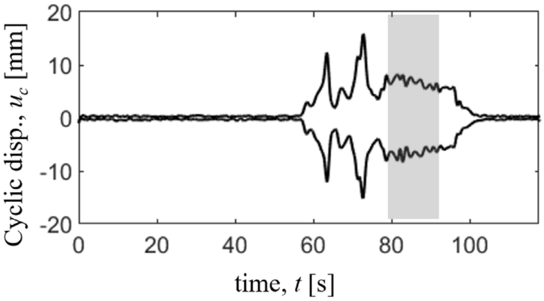

Fig. 12. Time-history response of pile T6: Envelope of maximum and minimum cyclic displacements. The gray background highlights the interval in which driving is ongoing.

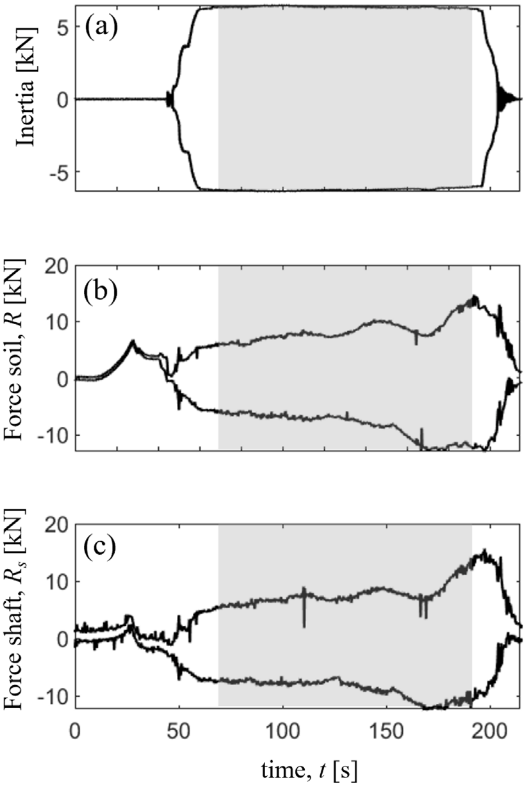

Fig. 13. Time-history response of pile T1. Envelope of maximum and minimum forces: (a) inertia forces, (b) soil reaction forces, and (c) shaft reaction forces. The gray background highlights the interval in which driving is ongoing.

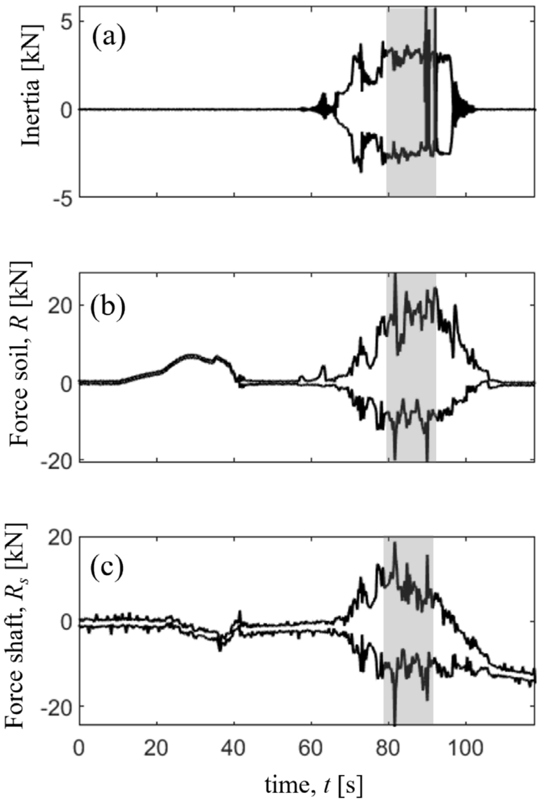

Fig. 14. Time-history response of pile T6. Envelope of maximum and minimum forces: (a) inertia forces, (b) soil reaction forces, and (c) shaft reaction forces. The gray background highlights the interval in which driving is ongoing.

4.1. *Results of total stress sensors*

Fig. 15 illustrates the evolution of the total stresses recorded by the sensors during penetration. The results are quite similar between the two pairs of sensors. The sensors mounted on the outer shaft show low-stress oscillations, while those on the inner shaft exhibit much higher extremes. The figure also includes the equivalent stress distribution of fluidized soil, with a unit weight of approximately 18 $\mathrm{kN/m^3}$. It is noteworthy that the stress measurements on the outer shaft closely follow this distribution, whereas those on the inner shaft show a wider range of variation but still oscillate around the same stress distribution.

It is worth mentioning that pile T8 is installed at a slow velocity. Other piles, installed at higher velocities, may have exhibited different stress distributions.

5. Overall test results during driving

This section describes all test results during driving. The results are divided into two subsections focusing on the tip response and shaft response, respectively.

5.1. *Tip response during driving*

This section illustrates the response of the tip during pile driving. The tip resistance is computed as follows:

$$\sigma_\mathrm{t} = \frac{R_\mathrm{t}}{\pi D_\mathrm{p} t_\mathrm{p}} \tag{5}$$

The tip stress σ_t during driving is typically correlated with the cone resistance q_c at the same depth, e.g., [38]. The ratio $\sigma_\mathrm{t}/q_\mathrm{c}$ is illustrated

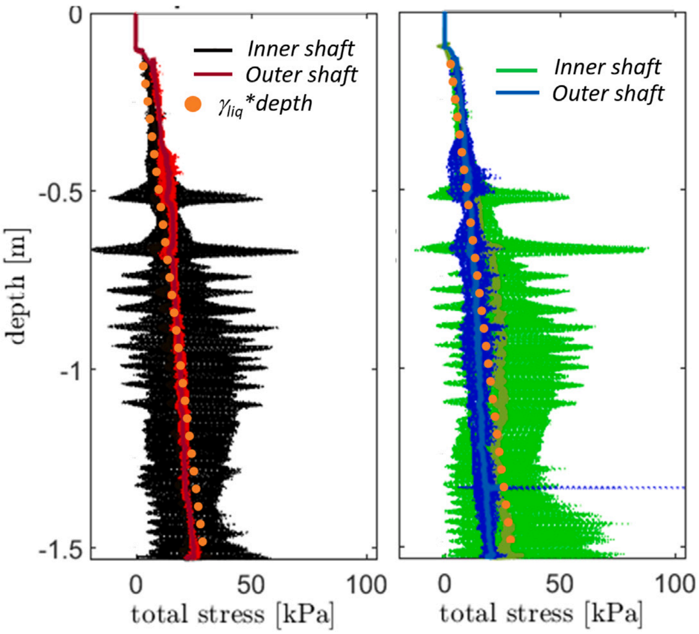

Fig. 15. Results of the total stress installed on pile T8, on the inner and outer shaft as function of the sensor depth.

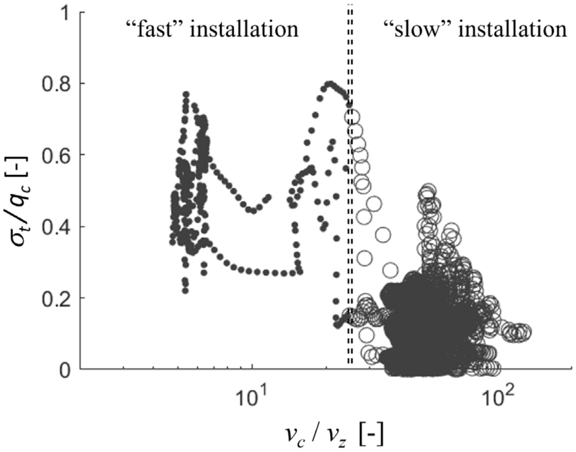

Fig. 16. The ratio σ_t/q_c as function of v_c/v_z. Filled markers for *fast installation* and unfilled for *slow installation*.

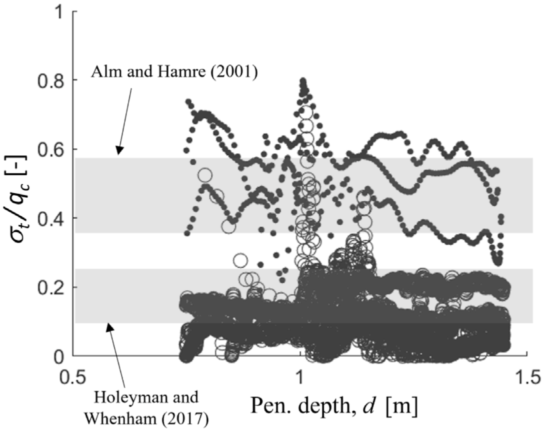

Fig. 17. Evolution of the ratio σ_t/q_c with penetration depth. Filled markers for *fast installation* and unfilled for *slow installation*.

Fig. 16, as a function of the dimensionless parameter v_c/v_z, where v_c is the amplitude of the cyclic velocity and v_z is the penetration velocity. In all tests, the pile tip moves both downward and upward during vibration, since $v_c/v_z > 1$. The majority of the data points are located in two distinct regions: one with the ratio $v_c/v_z > 35$ and one with $v_c/v_z < 7$. For $v_c/v_z > 35$, the cyclic velocities are significantly greater than the penetrating velocity; this regime is referred to as *slow installation*. Conversely, if $v_c/v_z < 7$, the regime is described as *fast installation*.

In Fig. 16, the boundary between the two groups is set arbitrarily at $v_c/v_z = 25$, as few data points fall between $v_c/v_z = 7$ and 35. The marker styles in these two regions differ as follows: filled markers represent *fast installation*, while unfilled markers denote *slow installation*.

The ratio σ_t/q_c is illustrated in Fig. 17, as function of the penetration depth. The style of the markers is consistent with the one used in Fig. 16. Notably, for each pile, the values of σ_t/q_c remain fairly constant with depth, even at shallow depths where the relative density is not uniform (i.e., depth shallower than 1 m).

In *fast installation* regime, the ratio σ_t/q_c is mostly varying between 0.3 and 0.7. These values align with the findings of [38], who reported a value of σ_t/q_c between 0.35 and 0.55 for impact-driven piles in coarse-grained soils (from loose to very dense sand). Furthermore, a value of $\sigma_t/q_c = 0.5$ has been corroborated by medium-scale field tests of vibratory driving in sand [34].

In *slow installation* regime, the ratio σ_t/q_c is below 0.25, much lower than *fast installation* regime. Holeyman and Whenham [39] proposed an approach to estimate the tip bearing capacity for vibro-driving, as follows:

$$\frac{\sigma_t}{q_c} = \frac{q_c - q_{c,l}}{q_c} e^{-a_p/g} + \frac{q_{c,l}}{q_c} \tag{6}$$

where $q_{c,l}$ is the cone resistance of the liquefied soil and a_p is the peak pile acceleration, normalized by the acceleration of gravity g. The value of $q_{c,l}$ is calculated as follows:

$$\frac{q_{c,l}}{q_c} = \left(1 - \frac{1}{\Lambda}\right) e^{-c_b/R_f} + \frac{1}{\Lambda} \tag{7}$$

where Λ is a degradation parameter, which is higher for saturated and loose sand, and it is chosen in the range between 4 and 10. The friction ratio R_f is measured in a CPT test, and c_b is an empirical parameter defining the degradation level of the tip reaction and varies between 0.015 and 0.02 for sand. In the experimental campaign, the values of a_p vary between 7 and 15 g, and R_f is approximately 0.004. This leads to $\sigma_t/q_c \simeq 1/\Lambda = 0.1 \sim 0.25$, which is in good agreement with the experimental findings presented in Fig. 17 for *slow installation* regime.

5.2. Shaft response during driving

The shaft reaction force is computed as:

$$R_s(d) = \pi D_p \int_0^d \tau_s(z,d)\,dz \tag{8}$$

where d is the tip embedment in the soil, and $\tau_s(z,d)$ is the soil shear stress along the shaft, which depends on the tip embedment d and the vertical coordinate along the pile length z (with $z \leq d$). The shear stress resistance along the shaft can be computed as:

$$\tau_s(z,t) = \mu_s \left(\sigma'_{n,o}(z,d) + \sigma'_{n,i}(z,d)\right) \tag{9}$$

where μ_s is the friction coefficient between pile and soil, and $\sigma'_{n,i}(z,d)$, $\sigma'_{n,o}(z,d)$ are the normal effective stresses acting on the inner and outer pile walls, respectively. However, since the normal stresses acting on the shaft are generally unknown, it is common practice to relate τ_s to the cone resistance q_c through a coefficient β, as follows:

$$\tau_s(z,d) = \beta(z,d) q_c(z) \tag{10}$$

where β is the lateral stress coefficient and q_c is the cone tip resistance measured by the CPT.

In this experimental campaign, the coefficient β cannot be determined directly from the experimental data, since there are no local measurements of the τ_s on the pile shaft. For that reason, an average value of the lateral coefficient, $\bar{\beta}$ (the overline indicates the averaged quantity), is defined as the pile penetrates into the ground, as follows:

$$\bar{\beta}(d) = \frac{R_s(d)}{(d-d_0)\pi D_p \bar{q}_c(d)} \tag{11}$$

where $\bar{q}_c(d)$ is the average value of the cone resistance between the tip embedment d and the self-penetration embedment d_0, and it is computed as follows:

$$\bar{q}_c(d) = \frac{\int_{d_0}^{d} q_c(z)\,dz}{\int_{d_0}^{d} dz} = \frac{\int_{d_0}^{d} q_c(z)\,dz}{d - d_0} \tag{12}$$

Substituting Eq. (12) into Eq. (11) leads to the following equation:

$$\bar{\beta}(d) = \frac{R_s(d)}{\pi D_p \int_{d_0}^{d} q_c(z)\,dz} \tag{13}$$

The integral at the denominator is calculated when the pile tip penetrates deeper than $d_0 = 20$ cm, which is reached by the self-weight of the pile and the vibro-hammer. The material above this depth is loosely packed with low shear strength, and therefore, the corresponding contribution to the shaft is considered negligible.

Fig. 18 shows the evolution of $\bar{\beta}$ with penetration depth, for both *"fast"* and *"slow"* installation. The results are presented for three regimes of installation frequencies: high frequency ($f > 30$ Hz), low frequency ($f < 20$ Hz), and medium frequency for values in between. In general, the value of $\bar{\beta}$ tends to decrease with increasing penetration depth. For *fast* installation, there is minimal dependency on loading frequency, as the curves nearly overlap. In contrast, for *slow* installation, a more pronounced dependency on loading frequency (and consequently on the cyclic amplitude $|u_c|$) is observed. At any given penetration depth, higher loading frequency (i.e., lower $|u_c|$) results in higher values of $\bar{\beta}$, approaching those observed for *fast* installation. Conversely, as the frequency decreases, $\bar{\beta}$ values generally become lower at the same penetration depth.

These insights are further supported by Fig. 19, which depicts the dependency of $\bar{\beta}$ on the cyclic amplitude $|u_c|$ for both installation methods. For *fast* installation, no dependency on $|u_c|$ is observed, whereas for *slow* installation, $\bar{\beta}$ clearly decreases as $|u_c|$ increases.

The variation of $\bar{\beta}$ as a function of the number of cycles (N) is shown in Fig. 20. For both *fast* and *slow* installation, $\bar{\beta}$ decreases with the number of cycles. At almost all number of cycles, higher loading frequency results in higher values of $\bar{\beta}$, with very few exceptions.

6. Back calculation of soil resistance during driving

This section provides an attempt to estimate the lateral stress coefficient β based on the experimental results.

The lateral stress coefficient, $\beta(z,d)$ is in general a function of several parameters:

$$\beta(z,d) = g\left(z, d, \sigma'_{v0}(z), D_r(z), |u_c(d)|, f(d), N(z,d)\right) \tag{14}$$

where $\sigma'_{v0}(z)$ is the initial vertical effective stress, $D_r(z)$ is the relative density of the soil, $|u_c(d)|$ is the peak amplitude of the cyclic vertical displacement, f is the driving frequency, and $N(z,t)$ is the number of loading cycles at each soil elevation. Further dependencies can be considered with an increasing degree of complexity, but the preceding ones are considered the most basic ones.

Key observations from the experimental data are as follows:

1. *Limited Variation in Initial Stress*: there is insufficient data to establish a dependency between $\beta(z,t)$ and $\sigma'_{v0}(z)$, as the variation in the initial stress is extremely limited.
2. *Uniform Relative Density* : the relative density during the tests was very similar; therefore, there is not enough data to establish a dependency between $\beta(z,t)$ and $D_r(z)$.
3. *Constant Penetration Velocity* : the piles penetrate the soil at a constant velocity (v_z), which is governed by the crane speed.
4. *Coupled Amplitude and Frequency* : the vibro-hammer used for all tests had a constant eccentric moment. As a result, the cyclic amplitude $|u_c|$ and the loading frequency f are closely related, and the current dataset cannot provide insight into both factors. Therefore, the effect of these two factors cannot be easily distinguished in this study.
5. *Shallow Sand Layer and Limited Data* : the piles were installed in a shallow sand layer with a penetration depth of about 1.5 m, where the top 0.75 m consisted of loosely packed sand. The back-calculation was performed only in the last 0.75 m due to a lack of more detailed data.

Given these considerations, the lateral coefficient $\beta(z,d)$ is expressed as follows:

$$\beta(z,d) = g\left(z, d, |u_c(d)|, N(z,d)\right) \tag{15}$$

This expression can be further simplified as:

$$\beta(z,d) = \beta_1 \cdot \beta_2\left(z, d, |u_c(d)|, N(z,d)\right) \tag{16}$$

where β_1 is a constant value and β_2 is a function of z, d, $|u_c|$ and N. In principle, β_1 and β_2 can take any values or forms, provided the model predictions align well with the experimental data.

An estimate for factor β_1 can be derived from the expression of [40]:

$$\beta_1 = 0.0132 \cdot \tan\,\delta \cdot \left(\frac{p'_0}{p_a}\right)^{0.13} \tag{17}$$

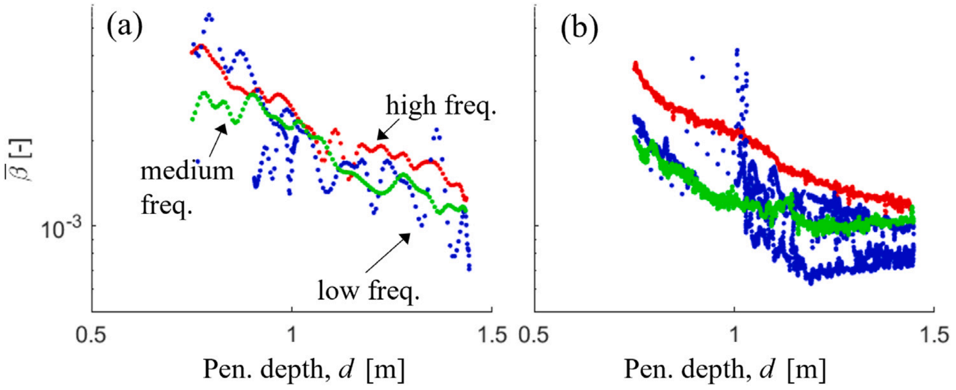

Fig. 18. Evolution of $\bar{\beta}$ with penetration depth (d). (a) *"fast"* installation and (b) *"slow"* installation. High frequency (f > 30 Hz), low frequency (f < 20 Hz), and medium frequency for values in between. Note that the vertical axis is presented on a logarithmic scale to emphasize variation across orders of magnitude. .

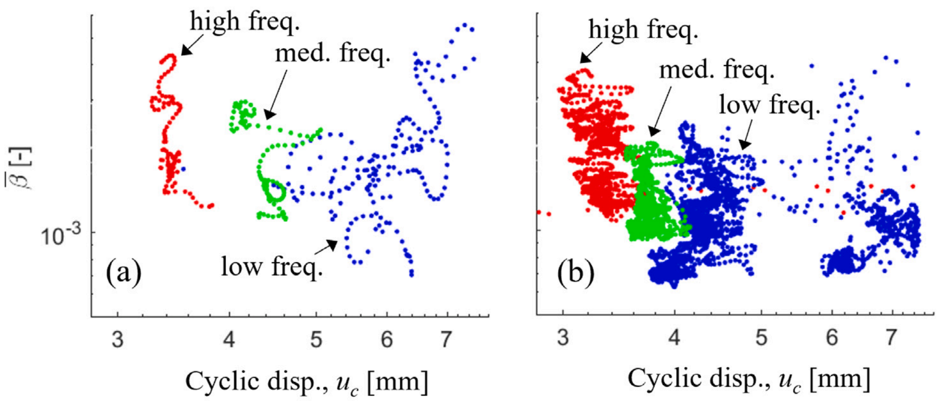

Fig. 19. Evolution of $\bar{\beta}$ with cyclic displacement (u_c). (a) *"fast"* installation and (b) *"slow"* installation. High frequency (f > 30 Hz), low frequency (f < 20 Hz), and medium frequency for values in between. Note that the vertical axis is presented on a logarithmic scale to emphasize variation across orders of magnitude. .

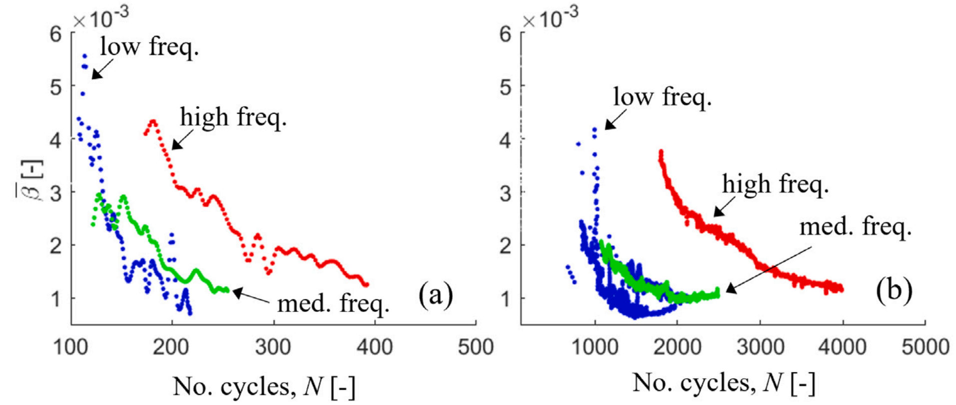

Fig. 20. Evolution of $\bar{\beta}$ with number of cycles (N). (a) *"fast"* installation and (b) *"slow"* installation. High frequency (f > 30 Hz), low frequency (f < 20 Hz), and medium frequency for values in between.

where $\tan\delta$ is the friction coefficient for the pile-shaft contact interface. Following the recommendations of [40], we consider $\delta = \phi - 5\ deg = 25\ deg$. By varying k_0 between 0.7 and 1.3, β_1 ranges from 4.3×10^{-3} to 4.9×10^{-3} over depth interval from 0.75 m and 1.5 m, with an average value of 4.6×10^{-3}. From medium-scale vibratory pile driving tests, Tsetas et al. [34] have obtained a value of $\beta_1 = 0.012$, which was also confirmed by axial-torsional vibratory driving tests at the same sandy site [41].

For β_2, various functional forms can be assumed. This paper evaluates three options, which are used to compute an analytical solution for $\bar{\beta}$ under the assumption that the cone resistance increases linearly with depth, i.e., $q_c(z) = m \cdot z$, where m is the rate of increase of q_c with depth.

The complete derivation is illustrated in Appendix, while the following presents a summary:

1. *Exponential Degradation with Depth:*

   $$\beta_2(z,d) = \alpha + (1-\alpha)\mathrm{e}^{-K(d-z)} \tag{18}$$

   where α is the ultimately degraded friction coefficient, and K is a memory parameter controlling the rate of degradation. This is the expression of friction fatigue proposed by Alm and Hamre [40]. The corresponding $\bar{\beta}$ can be calculated as follows:

   $$\bar{\beta}(d) = \beta_1 \left[\alpha + \frac{2(1-\alpha)}{K^2(d^2-d_0^2)}\left(Kd - 1 - d_0 K\mathrm{e}^{-K(d-d_0)} + \mathrm{e}^{-K(d-d_0)}\right)\right] \tag{19}$$

2. *Exponential Degradation with Loading Cycles:*

   $$\beta_2(N(z,d)) = \alpha + (1-\alpha)\mathrm{e}^{-A\cdot N(z,d)} \tag{20}$$

   where A is a memory parameter that governs degradation as a function of the number of loading cycles, N. This expression of friction fatigue has been proposed by Tsetas et al. [34]. A similar concept of degradation with respect to the number of cycles had already been experimentally observed by Moriyasu et al. [8], who reported the evolution of frictional properties under cyclic loading conditions. Since all tests are performed at constant v_z and f, the corresponding $\bar{\beta}$ has the same form as Eq. (19) with $K = A\ f/v_z$.
3. *Empirical expression based on [38]*

   $$\beta_2 = \hat{\beta}\ z^{0.13} \tag{21}$$

   where $\hat{\beta}$ is a constant reduction factor to the initial unit shaft resistance. The corresponding $\bar{\beta}$ is:

   $$\bar{\beta}(d) = 0.00428\ \hat{\beta} \tag{22}$$

The empirical expression of β_2, based on [38], was adopted by [6] to back-calculate the vibro-installations of three onshore monopiles with diameters ranging from 1.22 m to 0.76 m. In their simulation, friction fatigue was not included; instead, a constant reduction factor ($\hat{\beta} = 1/7$) was applied to both the initial unit shaft and unit toe resistance, yielding a good match with their installation data. However, Eq. (22) does not account for any dependency of $\bar{\beta}$ on penetration depth, as observed in Fig. 18. In these tests, $\bar{\beta}$ typically decreases with depth, from approximately 4×10^{-3} to 7×10^{-4}, except during *slow* installation tests at low loading frequencies, where it remains semi-constant. To align with the values shown in Fig. 18, Eq. (22) would require $\hat{\beta}$ values ranging from 1 to 1/5, which are higher than the value of 1/7 proposed by [6].

The performance of the other two functional forms (Eq. (18) and (20)) is assessed below, for *fast* and *slow* installation tests, respectively.

6.1. Fast installation

For *fast* installation, β_2 does not depend on $|u_c|$ based on the test data. The expression for friction fatigue proposed by [40] is adopted here (Eq. (18)), and a comparison between experimental data and back-calculated analytical models is presented in Fig. 21a and 22a.

Following the approach of Holeyman and Whenham [39], the lateral coefficient at liquefiable state can be estimated as:

$$\beta_{\mathrm{liq}} = \beta_1 \cdot \alpha = R_{\mathrm{f}} \left[\left(1-\frac{1}{\Lambda}\right)\ \mathrm{e}^{-c_{\mathrm{s}}/R_{\mathrm{f}}} + \frac{1}{\Lambda}\right] \tag{23}$$

where the recommended value of c_s is 0.06. For $R_{\mathrm{f}} = 0.004$, the ratio $\alpha \simeq R_{\mathrm{f}}/(\Lambda\ \beta_1)$, and for $\Lambda = 4 \sim 10$ and $\beta_1 = 4.6\ 10^{-3}$, the ratio α ranges between 0.21 and 0.08. In this comparison, three set of parameters are selected:

- Parameter set 1: $\beta_1 = 0.0046$, $\alpha = 0.15$, and $K = 6$.
- Parameter set 2: $\beta_1 = 0.0046$, $\alpha = 0.0$, and $K = 4$.
- Parameter set 3: $\beta_1 = 0.012$, $\alpha = 0.0$, and $K = 12$.

The value of K is adjusted to best fit the values of $\bar{\beta}$ obtained from the experimental data. For a given set of parameters, the use of Eq. (18) produces a single curve in Fig. 21a to describe the evolution of $\bar{\beta}$ with tip depth. Conversely, in Fig. 22a, the use of Eq. (18) generates multiple curves depending on the loading frequency of the test.

It is observed that, although all parameter sets provide satisfactory agreement with the experimental data in both Figs. 21a and 22a, parameter set 3 offers better agreement as it captures the steeper decay with penetration depth and the number of cycles.

6.2. Slow installation

For *slow* installation, Eq. (20) is used, which does not depend on $|u_c|$. For a given set of parameters, this expression for friction fatigue produces different curves in both Fig. 21b, while generating a single curve in Fig. 22b.

In this set of tests, the parameter $A = 0.0038$ is chosen to best fit the response of parameter set 3 at high loading frequencies. Using this parameter set, for a loading frequency of 35 Hz and a penetrating velocity $v_z = 1.1$ cm/s (typical of slow installation), the resulting value of K is 12, calculated using $K = A\ f/v_z$. This value is identical to the one obtained for high loading frequencies. As the loading frequency decreases, the value K decreases, leading to higher value of $\bar{\beta}$. However, this trend is opposite to the behavior observed in the experimental data.

Overall, the expression for friction fatigue described in Eq. (20) does not seem realistic when compared against the experimental data. Eq. (20) employs a coefficient A to describe friction fatigue, which is independent of the loading frequency (or $|u_c|$). To better capture the experimental evidence — characterized by different curves in both Figs. 21b and 22b -it is hypothesized that the coefficient A may not be constant but could increase as $|u_c|$ increases. However, at this stage, the experimental data are insufficient to draw definitive conclusions about the type of relationship that is most appropriate to capture friction fatigue in *slow* installation regime.

6.3. Discussion

Given the previous consideration, it is important to acknowledge that friction fatigue is not solely a function of the input loading parameters, but it is strongly dependent on the mechanical response of the surrounding soil. As expressed in Eq. (14), the lateral stress coefficient (β) – governing shaft resistance – depends on a set of variables such as relative density, amplitude of pile motion, in-situ effective stress, and accumulated loading cycles. These variables define the stress state of the soil in the pile vicinity, which dynamically evolves during installation and governs the degradation mechanism which manifests through plastic strains, excess pore pressure development, and/or non-linear material damping. Furthermore, these quantities are also associated with the energy dissipated into the soil, a quantity that can in itself be a control variable for friction fatigue as observed by Moriyasu et al. [8].

However, most of these parameters are not accessible in advance, nor can they be decoupled from one another in installation tests. For instance, pile motion amplitude, penetration rate and excess pore pressures emerge as the result of the coupled soil–structure interaction process. These quantities vary with depth, time, and installation settings while controlling the friction fatigue mechanism. Therefore, a comprehensive understanding of the role of soil properties and its mechanical response in friction fatigue demands a tailored and dedicated investigation, i.e. one that combines controlled variations in stress state and repetitive installation tests under well-monitored yet varying conditions. Building such a dataset across soil types, stress

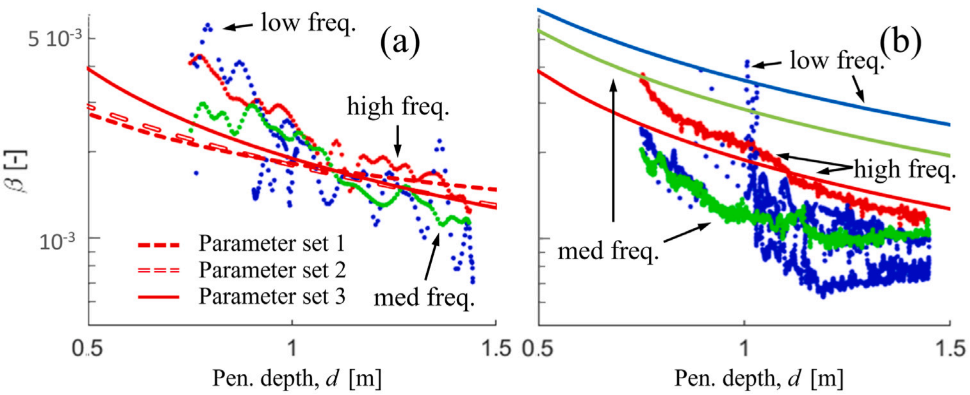

Fig. 21. Evolution of $\bar{\beta}$ with penetration depth (d). (a) *"fast"* installation and (b) *"slow"* installation. The comparison includes experimental data and back-calculated analytical models: Eq. (18) for *"fast"* installation and Eq. (20) for *"slow"* installation. Different colors represent different frequency ranges, from low to high. Note that the vertical axis is presented on a logarithmic scale to emphasize variation across orders of magnitude. .

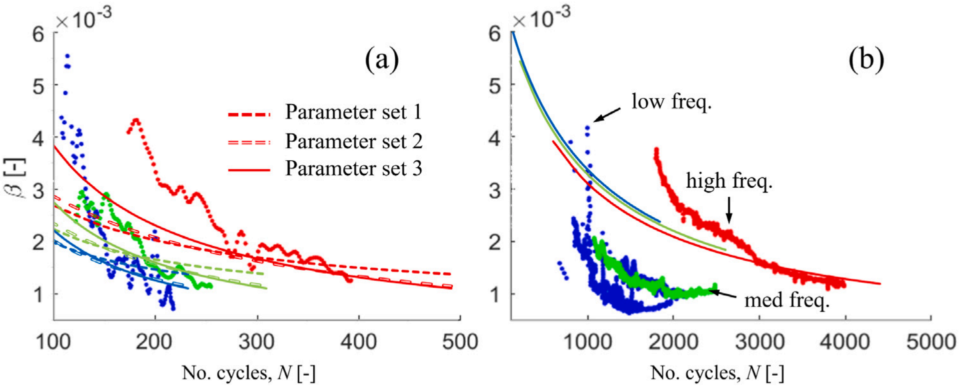

Fig. 22. Evolution of $\bar{\beta}$ number of cycles (N). (a) *"fast"* installation and (b) *"slow"* installation. The comparison includes experimental data and back-calculated analytical models: Eq. (18) for *"fast"* installation and Eq. (20) for *"slow"* installation. Different colors represent different frequency ranges, from low to high.

histories, and loading configurations is essential to establish robust and generalizable models for friction fatigue in offshore vibratory pile driving.

Given the complex and dynamic nature of friction fatigue discussed above, it is important to frame the contribution of this study accordingly. To date, there is no widely adopted/validated friction fatigue model for vibratory driving. Our work offers a systematic experimental investigation into the evolution of the lateral stress coefficient (β) during driving, under various installation settings.

In this regard, our approach aims to showcase a benchmarking strategy, comparing our findings against established friction fatigue frameworks from impact pile driving [40] and more recent exploratory work for vibratory loading [8,34]. It is deemed that this is an essential step to align future developments with a common reference framework, facilitating model validation and generalization. Overall, the development of a friction fatigue model applicable to vibratory pile driving is essential; for that purpose, research efforts should be grounded in diverse datasets, thus limiting potential overfitting to specific conditions.

7. Conclusions

This study presented the results of lab-scale experiments investigating the vibro-installation of tubular piles under controlled conditions. The findings provide valuable insights into the interaction between pile and soil during vibratory driving, addressing critical gaps in understanding the physics of the driving process. These results contribute to the broader goal of optimizing offshore monopile installation and support future development of predictive models for vibratory pile behavior. The following key conclusions are drawn:

1. *Driving Frequency and Penetration Efficiency:* The vibratory driving frequency influences soil resistance and installation dynamics. In the present setup, low frequencies are associated with higher cyclic pile displacements, and effectively lead to lower soil resistance during slow installations. In contrast, high frequencies result in lower cyclic displacements in the present hammer–pile–soil setup and lead to larger inferred soil resistance. It is noted that these findings are largely affected by the crane control; allowing the piles for the different tests to showcase different penetration rates will possibly alter the measured soil reaction. The observed trends underscore the importance of appropriately choosing both frequency and amplitude to optimize pile drivability and installation efficiency.
2. *Tip and Shaft Response:* The pile tip resistance depends on the ratio of cyclic to penetration velocities (v_c/v_z), with lower ratios in fast installations producing tip stresses similar to those observed in impact-driven piles. The lateral stress coefficient ($\bar{\beta}$), defined as the ratio between the shaft force and the product of the shaft area and the average cone resistance along the pile shaft, decreases with penetration depth. In fast installations, $\bar{\beta}$ appears largely independent of loading frequency and cyclic displacements. However, friction fatigue still plays a role, as the local lateral coefficient (β) at a given depth decreases with the distance from the pile tip during penetration. In slow installations, the impact of friction fatigue is more pronounced. The local lateral coefficient (β) strongly depends on cyclic displacement amplitude and loading frequency, leading to greater reductions in shaft resistance. This results in higher variability in $\bar{\beta}$, reflecting the cumulative effects of friction fatigue along the pile shaft.

3. *Prediction Models for Friction Fatigue:* The present findings experimentally confirm the central role of friction fatigue in shaft resistance degradation during vibratory installation. For fast installations, models assuming minimal dependency on cyclic displacement and frequency align well with observed behaviors. In contrast, slow installations require models that incorporate pronounced dependencies on dynamic loading conditions. These insights highlight the need for refined models that incorporate the coupled effects of driving parameters and soil response, in particular for the so-called slow installation cases which are more representative of vibratory driving in engineering practice.
4. *Practical Implications:* Vibratory driving is a sustainable and efficient alternative to impact driving, particularly for large-diameter monopiles. The experimental observations confirm its potential to reduce soil resistance and installation time, under appropriate driving conditions. These results can inform design and optimization of vibratory systems in offshore wind applications. Nonetheless, the current study is based on lab-scale tests, and therefore subject to scale effects. Mechanisms such as shaft friction, tip resistance, and soil plugging may evolve differently at full scale due to variations in stress distributions and pile dimensions. Extrapolation of the present findings to field conditions should be approached with care, and further validation through medium- or full-scale testing is recommended.

Overall, this study presents a systematic experimental quantification of tip reaction and friction fatigue along the pile shaft during vibratory pile driving. The comparison with existing friction fatigue frameworks serves to benchmark such approaches in the light of new field observations. In that manner, a robust and generalizable friction fatigue framework can be built, provided that future research extends to broader soil types, stress conditions and scales.

CRediT authorship contribution statement

Mario Martinelli: Writing – original draft, Visualization, Validation, Software, Methodology, Investigation, Formal analysis, Data curation, Conceptualization. **Athanasios Tsetas:** Writing – original draft, Validation, Methodology, Investigation, Formal analysis, Data curation, Conceptualization. **Andrei B. Fărăgău:** Writing – review & editing, Investigation. **Andrei Metrikine:** Writing – review & editing, Resources, Project administration, Funding acquisition. **Apostolos Tsouvalas:** Writing – review & editing, Resources, Project administration, Funding acquisition.

Declaration of competing interest

The authors declare that they have no known competing financial interests or personal relationships that could have appeared to influence the work reported in this paper.

Acknowledgments

This paper is part of the SIMOX joint industry project in the framework of the GROW Research Programme. The project is funded by Topsector Energiesubsidie from the Dutch Ministerie van Economische Zaken en Klimaat, grant number MOOI12001, and financial/technical support from the following partners, in alphabetical order: Boskalis, CAPE Holland, Deltares, Delft Offshore Turbine (DOT), Delft University of Technology, GBM Works, Heerema Engineering Solutions, Heerema Marine Contractors, IQIP, Ocean Winds, Ørsted, RWE, Seaway7, Shell, Siemens Gamesa Renewable Energy, Sif Netherlands, TNO, TotalEnergies, Van Oord, Vattenfall. The contribution to the tests of, in alphabetical order, Bastiaan van der Veen, Brice Dijksman, Cedrik de Roo, Danko Boonstra, Jaap Elstgeest, Kees van Beek and Marcel Busink, is also appreciated.

Appendix. Derivation of analytical expressions for friction fatigue

If a (mono)pile is embedded due to self-weight into the ground for d_0, the self-weight load is primarily carried by the tip reaction force, with a negligible contribution from the shaft. During subsequent driving, the average lateral coefficient along the shaft can be computed as follows:

$$\bar{\beta}(d) = \frac{R_s(d)}{\pi D_{\mathrm{p}} \int_{d_0}^{d} q_c(z)\,dz} = \frac{\int_{d_0}^{d} \tau_{\mathrm{s}}(z,d)\,\mathrm{d}z}{\int_{d_0}^{d} q_c(z)\,dz} = \frac{\int_{d_0}^{d} \beta(z,d) q_{\mathrm{c}}(z)\,\mathrm{d}z}{\int_{d_0}^{d} q_c(z)\,dz} \tag{A.1}$$

This section computes the analytical solution for the case of cone resistance being linear with depth, $q_c(z) = mz$, where m is the rate of increase of q_c with depth. Friction fatigue in pile driving refers to the degradation of the frictional resistance between the pile and the surrounding soil due to repetitive loading during the driving process. The lateral coefficient β is expressed as function of a product between a constant β_1 and a function β_2, as follows:

$$\beta(z,d) = \beta_1 \cdot \beta_2\,(z,d,N(z,d)) \tag{A.2}$$

where β_2 is function of depth (z), tip embedment (d), and number of cycles (N). The following subsections describe the analytical solutions for the case where (1) β_2 is only function of depth (z) and tip embedment (d), (2) β_2 is function of number of cycles $(N(z,d))$, and (3) β_2 is function of the only depth (z).

A.1. Exponential degradation with depth

$$\beta_2(d) = \alpha + (1-\alpha)\mathrm{e}^{-K(d-z)} \tag{A.3}$$

$$R_s(d) = \beta_1 \int_{d_0}^{d} \beta_2(z,d) \cdot mz\,dz \tag{A.4}$$

$$\int_{d_0}^{d} q_c(z)\,dz = \int_{d_0}^{d} mz\,dz = m\left(\frac{d^2}{2} - \frac{d_0^2}{2}\right) \tag{A.5}$$

$$R_s(d) = \beta_1 \int_{d_0}^{d} \left[\alpha + (1-\alpha)\mathrm{e}^{-K(d-z)}\right] \cdot mz\,dz \tag{A.6}$$

$$\begin{aligned} R_s(d) = \beta_1 \Bigg[& \int_{d_0}^{d} \alpha mz\,dz \\ & + \int_{d_0}^{d} mz(1-\alpha)\mathrm{e}^{-K(d-z)}\,dz \Bigg] \end{aligned} \tag{A.7}$$

$$\begin{aligned} R_s(d) = \beta_1 \Bigg[& \alpha m\left(\frac{d^2}{2} - \frac{d_0^2}{2}\right) + \\ & + \frac{m(1-\alpha)}{K^2}\left(Kd - 1 - d_0 K \mathrm{e}^{-K(d-d_0)} + \mathrm{e}^{-K(d-d_0)}\right) \Bigg] \end{aligned} \tag{A.8}$$

$$\bar{\beta}(d) = \beta_1 \left[\alpha + \frac{2(1-\alpha)}{K^2(d^2 - d_0^2)}\left(Kd - 1 - d_0 K \mathrm{e}^{-K(d-d_0)} + \mathrm{e}^{-K(d-d_0)}\right)\right] \tag{A.9}$$

It is interesting to note that $\bar{\beta}(d)$ is independent of m, which is the rate of increase of q_c with depth. In general, $\bar{\beta}(d)$ is always greater than $\bar{\beta}_{min} = \beta_1\ \alpha$, which is attained when $d \gg d_0$. Consequently, although these two values (β_1 and α) are independent of each other, selecting a representative value for both must be done carefully to ensure that $\bar{\beta}(d)$ aligns with the experimental data as much as possible.

A.2. Exponential degradation with loading cycles

As the number of shear cycles increases due to each hammer blow or revolution of the vibro-hammer, the skin friction gradually approaches a minimum residual value or lower limit. The lateral coefficient $\beta_2(z,d)$ is then expressed as:

$$\beta_2(z,d) = \alpha + (1-\alpha)\mathrm{e}^{-AN(z,d)} \tag{A.10}$$

where A is the degradation rate constant. If the tests are performed at constant penetration velocity and at constant loading frequency, the number of cycles can directly be computed as $N(z,d) = \frac{f}{v_z}(d-z)$. It follows that β_2 yields:

$$\beta_2(z,d) = \alpha + (1-\alpha)\mathrm{e}^{-K(d-z)} \tag{A.11}$$

with $K = Af/v_z$.

A.3. Empirical expression based on [38]

$$\tau_s(z) = \hat{\beta} \ \cdot \ 0.0132 \cdot \tan \ \delta \cdot \left(\frac{p'_0}{p_a}\right)^{0.13} \cdot mz \tag{A.12}$$

where $\hat{\beta}$ is the constant reduction factor to the initial unit shaft resistance. Following the definition of Eq. (A.2), the coefficients β_1 and β_2 are derived as:

$$\beta_1 = 0.0132 \cdot \tan \ \delta \cdot \ \left((1+2\ k_0)/30\right)^{0.13} \tag{A.13}$$

$$\beta_2(z) = \hat{\beta}\ z^{0.13} \tag{A.14}$$

where β_1 is a constant value and β_2 is only function of z.

The shaft reaction force is:

$$R_s(d) = m\ \beta_1 \int_{d_0}^{d} z^{1.13} \cdot dz = \frac{m\ \beta_1}{2.13}\ (d^{2.13} - d_0^{2.13}) \tag{A.15}$$

$$\bar{\beta}(d) = \frac{R_s(d)}{\int_{d_0}^{d} q_c(z)\,dz} = \frac{2\ \beta_1}{2.13}\ \frac{(d^{2.13} - d_0^{2.13})}{(d^2 - d_0^2)} \tag{A.16}$$

Following the recommendations of [40], $\delta \ = \ \phi - 5\ deg = 25\ deg$. The value of k_0 varies between 0.7 and 1.3 in the site. The ratio $\left((1+2\ k_0)/30\right)^{0.13} = 0.72 - 0.76$, and a value of 0.74 is considered in the calculations. The ratio $\frac{(d^{2.13}-d_0^{2.13})}{(d^2-d_0^2)}$ varies between 0.95 and 1.05 for $d_0 \ = \ 0.2\ m$ and for d between 0.5 and 1.5 m, therefore it is reasonable to assume that the ratio $\frac{(d^{2.13}-d_0^{2.13})}{(d^2-d_0^2)} \approx 1$. It follows that:

$$\bar{\beta}(d) = 0.00428\ \hat{\beta} \tag{A.17}$$

Data availability

Data will be made available on request.

References

[1] International Energy Agency. World energy outlook 2023. Technical report, Paris, France; 2023.

[2] Merchant ND. Underwater noise abatement: economic factors and policy options. Environ Sci Policy 2019;92:116–23.

[3] Tsouvalas A. Underwater noise emission due to offshore pile installation: A review. Energies 2020;13(12):3037.

[4] Achmus M, Schmoor KA, Herwig V, Matlock B. Lateral bearing behaviour of vibro-and impact-driven large-diameter piles in dense sand. Geotechnik 2020;43(3):147–59.

[5] Tsetas A. A unified modelling framework for vibratory pile driving methods [Ph.D. thesis], Delft University of Technology; 2023.

[6] Konstantinou M, Stathopoulou E, Luger D, Elkadi A. Driveability back-analyses of onshore vibratory and vibrojetting installation tests on tubular piles. In: Offshore technology conference. Houston: OTC; 2023.

[7] Lu W, Li B, Hou J, Xu X, Zou H, Zhang L. Drivability of large diameter steel cylinders during hammer-group vibratory installation for the Hong Kong–Zhuhai–Macao bridge. Engineering 2023;20:180–91.

[8] Moriyasu S, Kobayashi S, Matsumoto T. Experimental study on friction fatigue of vibratory driven piles by in situ model tests. Soils Found 2018;58(4):853–65.

[9] Jan De Nul. Formosa I offshore wind project. 2019, URL: https://www.jandenul.com/our-projects/offshore-windpark-formosa-1-phase-2-taiwan. (Accessed 17 February 2025).

[10] Formosa 2 Wind Power. Formosa II offshore wind project. 2023, URL: https://formosa2windpower.com/en/. (Accessed 17 February 2025).

[11] Renewables RWE. Kaskasi II offshore wind farm. 2022, URL: https://www.rwe.com/en/the-group/countries-and-locations/offshore-wind-farm-kaskasi/. (Accessed 17 February 2025).

[12] Offshore EWE. Riffgat offshore wind farm. 2012, URL: https://www.ewe.com/en/ewe-group/company/group-structure/offshore-windpark-riffgat. (Accessed 17 February 2025).

[13] BOEM. Coastal virginia offshore wind (CVOW). 2024, URL: https://www.boem.gov/renewable-energy/state-activities/CVOW-C. (Accessed 17 February 2025).

[14] Hai Long Wind. Hai long offshore wind project. 2024, URL: https://hailongoffshorewind.com/. (Accessed 17 February 2025).

[15] Moray West Offshore Wind. Moray west offshore wind farm. 2024, URL: https://www.moraywest.com/. (Accessed 17 February 2025).

[16] 4C Offshore. Yunlin offshore wind farm. 2024, URL: https://www.4coffshore.com/windfarms/taiwan/yunlin-taiwan-tw10.html. (Accessed 17 February 2025).

[17] Tsetas A, Tsouvalas A, Gómez S, Pisanò F, Kementzetzidis E, Molenkamp T, et al. Gentle driving of piles (GDP) at a sandy site combining axial and torsional vibrations: Part I - installation tests. Ocean Eng 2023;270:113453.

[18] Wang W, Brown MJ, Sharif YU, Davidson C, Ciantia MO. Centrifuge modeling of the installation advancement ratio effect on the cyclic response of a single-helix screw pile for floating offshore wind. J Geotech Geoenvironmental Eng 2025;151(1):04024133.

[19] Ørsted. Ørsted successfully pilots new technology that further optimises offshore wind monopile installation. 2024, URL: https://orsted.com/en/media/news/2024/07/orsted-successfully-pilots-new-technology-that-fur-13959650. (Accessed 17 February 2025).

[20] Elzinga J, Mesu A, van Eekelen E, Wochner M, Jansen E, Nijhof M. Installing offshore wind turbine foundations quieter: A performance overview of the first full-scale demonstration of the AdBm underwater noise abatement system. In: Offshore technology conference. OTC; 2019, D021S019R003.

[21] Klages E, Lippert S, von Estorff O. A noise-reduced impact hammer for offshore pile driving. In: Proceedings of meetings on acoustics, vol. 44, AIP Publishing; 2021.

[22] GROW. Sustainable installation of XXL monopiles (SIMOX). 2021, https://grow-offshorewind.nl/project/simox.

[23] Byrne T, Gavin K, Prendergast L, Cachim P, Doherty P, Pulukul SC. Performance of CPT-based methods to assess monopile driveability in north sea sands. Ocean Eng 2018;166:76–91.

[24] Machaček J, Staubach P, Tafili M, Zachert H, Wichtmann T. Investigation of three sophisticated constitutive soil models: From numerical formulations to element tests and the analysis of vibratory pile driving tests. Comput Geotech 2021;138:104276.

[25] Staubach P, Machaček J, Skowronek J, Wichtmann T. Vibratory pile driving in water-saturated sand: Back-analysis of model tests using a hydro-mechanically coupled CEL method. Soils Found 2021;61(1):144–59.

[26] Staubach P, Machaček J. Spatially mixed implicit–explicit schemes in hydro-mechanically coupled soil dynamics. Comput Geotech 2024;176:106811.

[27] Galavi V, Beuth L, Zuada Coelho B, Tehrani F, Holscher P, Van Tol F. Numerical simulation of pile installation in saturated sand using material point method. Procedia Eng 2017;175:72–9.

[28] Martinelli M, Galavi V, Elkadi A. Simulation of gentle pile driving (GDP) using the material point method. In: 20th international conference on soil mechanics and geotechnical engineering. 2022.

[29] Van Dorp R, Moscoso N, Bielefeld M, Verbeek G. Prediction and monitoring of installation of offshore foundation monopiles for windfarms. In: Offshore technology conference. OnePetro; 2019.

[30] Mazza N, Holeyman A. Frequency-penetration response spectrum on vibratory amplitude matching of monopiles. In: 10th international conference on stress wave theory and testing methods for deep foundations. ASTM International; 2019.

[31] Berghe JV, Holeyman A. Application of a hypoplastic constitutive law into a vibratory pile driving model. In: Proceedings of the international conference on vibratory pile driving and deep soil compaction. 2002, p. 61–8.

[32] Xiao Y, Ge Y. A numerical model of VPS for offshore wind turbine monopiles based on hypoplastic theory. Int J Numer Anal Methods Geomech 2022;46(4):697–716.

[33] Kaynia AM, Hebig J, Pein T, Shin Y. Numerical model for dynamic installation of large diameter monopiles. Soil Dyn Earthq Eng 2022;161:107393.

[34] Tsetas A, Tsouvalas A, Metrikine AV. A non-linear three-dimensional pile–soil model for vibratory pile installation in layered media. Int J Solids Struct 2023;269:112202. http://dx.doi.org/10.1016/j.ijsolstr.2023.112202.

[35] da Silva AP, Post M, Elkadi A, Kementzetzidis E, Pisanò F, et al. Effect of installation parameters and initial soil density on the lateral response of vibratory-driven monopiles: a laboratory study. In: Offshore site investigation geotechnics 9th international conference proceeding, vol. 1838, Society for Underwater Technology; 2023, p. 1838–46.

[36] Sibelco. URL: https://www.sibelco.com/en/locations/baskarp.

[37] Krogh L, Quinteros S, Engin HK, Lunne T. Revisiting interpretation of relative density from shallow depth CPTs in sand. Can Geotech J 2022;59(6):808–26. http://dx.doi.org/10.1139/cgj-2021-0200.

[38] Alm T, Hamre L. Soil model for driveability predictions based on CPT measurements. In: 15th int. conf. on soil mech & geotech engineering. 2001, p. 1297–302.

[39] Holeyman A, Whenham V. Critical review of the Hypervib1 model to assess pile vibro-drivability. Geotech Geol Eng 2017;35(5):1933–51.

[40] Alm T, Hamre L. Soil model for driveability predictions. In: Offshore technology conference. Houston: OTC; 1998.

[41] Tsetas A, Tsouvalas A, Metrikine AV. The mechanics of the gentle driving of piles. Int J Solids Struct 2023;282:112466.